JMEPEG (2010) 19:301–313
DOI: 10.1007/s11665-009-9482-y

1059-9495/$19.00

Reliability-Based Design Optimization for Durability of Ground Vehicle Suspension System Components

M. Grujicic, G. Arakere, W.C. Bell, H. Marvi, H.V. Yalavarthy, B. Pandurangan, I. Haque, and G.M. Fadel

(Submitted March 26, 2009)

The effect of materials processing- and component manufacturing-induced uncertainties in material properties and component shape and size on the reliability of component performance is investigated. Specifically, reliability of a suspension system component from a high-mobility multipurpose wheeled vehicle which typically can fail under low-cycle strain-based fatigue conditions is analyzed. Toward that end, the most advanced reliability-based design optimization methods available in the literature were combined with the present understanding of low-cycle fatigue durability and applied to the component in question. This entailed intricate integration of several computational tools such as multibody vehicle dynamics, finite-element simulations, and fatigue strain-life assessment/prediction techniques. The results obtained clearly revealed the importance of consideration of material property uncertainties in attaining vehicle performance of critical structural components in complex systems (e.g., a vehicle).

Keywords fatigue-controlled durability, material property uncertainties, probabilistic constraints, reliability-based design optimization (RBDO)

1. Introduction

Recent efforts of the U.S. Army have been aimed at becoming more mobile, deployable, and sustainable while maintaining or surpassing the current levels of lethality and survivability. Current battlefield vehicles have reached in excess of 70 tons due to ever increasing lethality of ballistic threats which hinders their ability to be readily transported and sustained. Therefore, a number of research and development programs are under way to engineer light-weight, highly mobile, transportable, and lethal battlefield vehicles with a target weight under 20 tons. Similar relative weight reductions are also being targeted for tactical military vehicle such as the high-mobility multipurpose wheeled vehicle (HMMWV) or mine-resistant ambush vehicle. To attain these goals, significant advances are needed in the areas of lightweight materials and lightweight, volumetrically efficient structures (e.g., multilayered structures made from high specific-strength metals and ballistic fiber structures infused with impact resistant epoxy polymer systems) as well as in the integration of multifunctional armor. However, as different light weighting approaches are being considered and tested, it has become clear that the issues associated with the durability (in particular, fatigue and corrosion-controlled durability) have to be addressed. That is, as the vehicles weight is being reduced (while maintaining their blast/ballistic survivability), it is critical to ensure that vehicle life time does not become governed by in-service-induced transient dynamic and cyclic loadings or by prolonged exposure to hot, humid, dusty, and other aggressive natural environmental conditions. In this work, only the issues associated with fatigue-controlled durability will be discussed.

The second topic that will be covered in this work is related to the concept of reliability of the engineering design. That is, as one applies engineering design-optimization methods and tools to determine the optimal size and shape for various vehicle components while ensuring a desired level of components performance (e.g., a desired fatigue life of the component), one must contend with the issues associated with material processing- and component manufacturing-induced variability/uncertainties in the key material/design parameters. That is, it must be recognized that when design-optimization techniques are used, the optimal deterministic designs typically lie on the *safe/fail* boundaries, also referred to as the *limit-state* boundaries (i.e., on the surfaces in the multidimensional design space which divide the design space into the *safe* and the *fail* regions). Consequently, an optimal deterministic design leaves practically no room for (material, manufacturing, assembly, etc. induced) uncertainties in the design variables while still ensuring a reliable design. To overcome the limitations associated with the deterministic design optimization approaches, new methods and tools commonly referred to as reliability-based design optimization (RBDO) have been developed over the last few years (Ref 1-4).

As will be shown later in greater detail, the RBDO approach entails evaluation of the probabilistic constraints. Simply stated, while the deterministic constraints are defined as nonequality conditions, e.g., "the maximum stress level within the component under investigation must not exceed the material yield strength," the corresponding probabilistic constraint is defined as "the probability that the maximum stress within the component exceeds the material yield strength is lower than a (small) acceptable failure-probability level." Clearly, to be able to evaluate the probability of failure associated with each

M. Grujicic, G. Arakere, W.C. Bell, H. Marvi, H.V. Yalavarthy, B. Pandurangan, I. Haque, and **G.M. Fadel**, International Center for Automotive Research CU-ICAR, Department of Mechanical Engineering, Clemson University, Clemson, SC 29634. Contact e-mail: mica.grujicic@ces.clemson.edu.

constraint of a design, the probability density function, PDF (or the associated cumulative distribution function, CDF), must be determined for each constraining function. While this is possible using Monte Carlo simulations, this approach is highly unpractical due to its prohibitively high computational cost and is not generally used. Instead, within the RBDO, the so-called first-order reliability methods (FORM) have been proposed (Ref 5-9).

Within the FORM methods, the evaluation of the probabilistic constraints does not require the knowledge of PDFs or CDFs and is simply carried out by evaluating the constraining function at the so-called most probable point (MPP) within the standard normal design space (referred to as the *u-space*, hereafter). That is, the design variables (as being assigned by the optimization algorithm) are first made mutually uncorrelated, then transformed into the corresponding standard normal variables (variables associated with a zero-mean and unit standard deviation normal distribution function). Then, one of the procedures (discussed later) is used to find the MPPs (one MPP for each constraint) and evaluate the corresponding constraining functions at their respective MPP. In other words, while within the deterministic design-optimization approach, both the objective function and the constraining relations are evaluated at the same (*mean*) levels of the design variables; within the FORM, the objective function is still evaluated at the mean values of the design variables (as assigned by the design-optimization algorithm) while the constraining relations are evaluated at the values of the design variables associated with the corresponding MPPs. As will be shown later, to find the MPP for each constraint, one must employ an additional optimization procedure within the standard normal design space. Thus, the RBDO involves two nested design-optimization procedures: the outer one governs the evolution of the design via the mean values of the design variables, whereas the inner one is used to determine the MPPs (one MPP for each constraint) associated with the given set of design-variable mean values. More details regarding the RBDO and the FORM will be provided in next section.

Fatigue-controlled durability of a prototypical suspension system component (i.e., the upper A-arm in the HMMWV) is investigated in this work. In principle, the fatigue-controlled life time of this component can be governed either by repeated stresses (i.e., *stress-cycle life*) or by repeated (plastic) strains (i.e., *strain-cycle life*) (Ref 10). While the overall level of stresses in the component is quite smaller than the material yield strength, very frequently, sections in the component are found in which (due to adjacent geometrical discontinuities, e.g., notches, or due to nearby connection points) the onset of plasticity is quite probable. Consequently, in this work, it is assumed that the fatigue life of the component in question is strain-cycle controlled. The necessary details regarding the strain-cycle fatigue-controlled life are presented in Section 2.2.

The main objective of this work is to demonstrate how the FORM methods can be coupled with a strain-life fatigue analysis to optimize shape and size of a prototypical suspension system automotive component with respect to minimizing component's mass while ensuring that the (probabilistic) fatigue-durability constraints are satisfied. The main cause for the probabilistic nature of the constraints is various materials processing- and component manufacturing-induced variability/uncertainties in material properties and the component size and/or shape. The second objective of this work is to demonstrate the concept of intimate integration of several computational tools such as multibody vehicle dynamics, finite-element simulations, material property databases, and fatigue strain-life assessment/prediction techniques in the course of material selection and design optimization for weight efficient, durable, and reliable critical automotive components.

The organization of the article is as follows: In Section 2.1, a brief overview is provided of the general formulation of the RBDO and of several FORM computational methods for determination of the MPP locations (used in the evaluation of probabilistic constraints). This is followed, in Section 2.2, by a brief discussion of strain-cycle fatigue durability in the presence of real in-service cyclic loads which are both of nonconstant amplitude and mutually nonproportional. Implementation of RBDO for strain-based fatigue durability is presented in Section 2.3. The results obtained in this work are presented and discussed in Section 3. The main conclusions resulting from this work are summarized in Section 4.

2. Computational Procedures

2.1 Reliability-Based Design Optimization

2.1.1 General Definition of the RBDO Problem. Within the design space defined by a set of design variables, d, and a set of associated random variables, X, the RBDO problem can be stated as:

$$\begin{aligned} &\textit{Minimize}: Cost(\underset{\sim}{\boldsymbol{d}}) \\ &\textit{Subjected to}: P(G_i \boldsymbol{d}(\underset{\sim}{\boldsymbol{X}})) \geq 0) - \Phi(-\beta_{t,i}) \leq 0, \quad i = 1, \ldots, N_{\mathrm{PC}}, \\ &\underset{\sim}{\boldsymbol{d}}^{\mathrm{L}} \leq \underset{\sim}{\boldsymbol{d}} = \mu(d(\boldsymbol{X})) \leq \underset{\sim}{\boldsymbol{d}}^{\mathrm{U}}, \quad \underset{\sim}{\boldsymbol{d}} \in \boldsymbol{R}^{N_{\mathrm{DV}}} \text{ and } \underset{\sim}{\boldsymbol{X}} \in \boldsymbol{R}^{N_{\mathrm{RV}}} \end{aligned} \tag{Eq 1}$$

where P denotes probability, G_i one of the N_{PC} probabilistic constraints, Φ the standard normal cumulative distribution function, $\beta_{t,i}$ the confidence limit (defined in terms of the number of standard normal deviations), and μ stands for the mean value. Superscripts L, U, N_{DV}, and N_{RV} denote lower limit, upper limit, the number of design variables, and the number of random variables, respectively, and $\boldsymbol{R}$ denotes a real-number set. It should be noted that throughout the article vector quantities are denoted using bold-face italicized symbols. Also, a distinction should be made between random design variables (e.g., component size and shape variables), $d(X)$, which are iterated during design optimization and the remaining random variables (a subset of X) which are associated with statistical uncertainty but do not vary with design (e.g., material properties).

Equation 1 simply states that the cost (e.g., the mass of a component) should be minimized while subjected to the (probabilistic) constraints that the probability for violating any of the constraints must not exceed the acceptable level of failure probability, $\Phi(-\beta_{t,i})$.

It should be noted that in Eq 1, the failure portion of the design space is associated with $G_i(\underset{\sim}{\boldsymbol{d}}(\boldsymbol{X})) \geq 0$ condition. Thus, the probability for failure is numerically equal to the corresponding multiple integral of the joint probability density function over the *fail* portion of the design space. Direct evaluation of this integral is prohibitively costly and is generally not done. Instead, one of the (approximate) FORMs is employed (discussed below in greater detail).

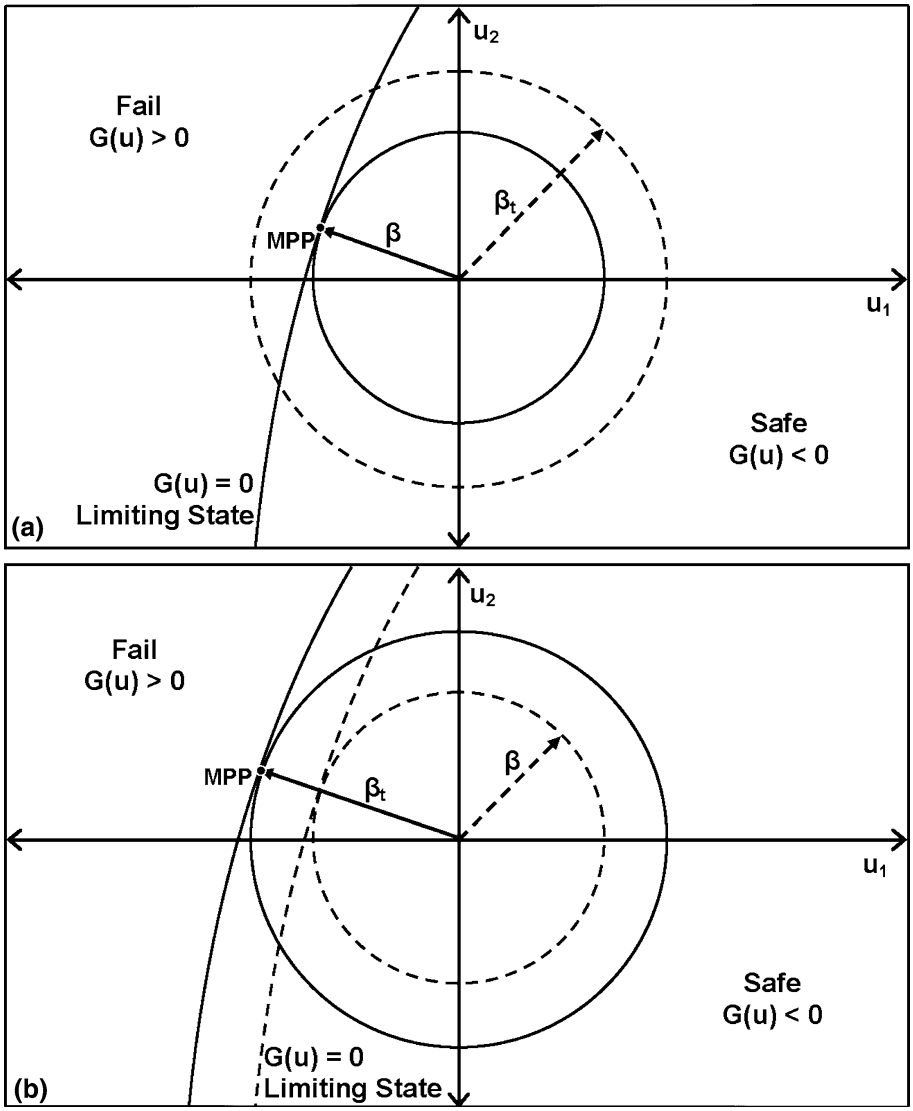

Fig. 1 Simple schematic of: (a) the reliability index approach (RIA) and (b) the performance measure approach (PMA) for a two design variable case. Please see text for nomenclature and for more details

2.1.2 The First-Order Reliability Methods. The first step in the FORM is to transform the set of random (and potentially correlated) design variables $d(X)$ into the corresponding set of uncorrelated standard normal variables, $\underset{\sim}{u}$. It should be next noted that, since the probability density function for each standard normal variable, $\boldsymbol{u}_i$, is defined as $f(\boldsymbol{u}_i) = (2\pi)^{-0.5}\exp(-\boldsymbol{u}_i^2/2)$, and the variables are uncorrelated, the joint probability density function is defined as: $f_u(\boldsymbol{u}) = \prod_{N_{RV}} f(\boldsymbol{u}_i)$. Consequently, in the standard normal distribution space, the loci of constant joint probability density function are (multidimensional) spheres centered at the *u-space* origin. The spheres radius is defined simply as: $\beta = |\underset{\sim}{u}| = (u_1^2 + u_2^2 + \cdots)^{1/2}$. One should also recognize that, within the *u-space*, the *safe* and the *fail* domains associated with each of the constraints are separated by the corresponding (multidimensional) *limit-state* surface.

Evaluation of the probabilistic constraints is next done within the *u-space* by employing either the so-called reliability index approach (RIA) or the performance measure approach (PMA) (Ref 5-9). To facilitate the understanding of the RIA and the PMA, simple schematics are provided for a RIA and a PMA case with two design variables and one probabilistic constraint in Fig. 1(a) and (b), respectively.

In qualitative terms, within the RIA, a point (i.e., the MPP) on the *limit-state*, $G(\boldsymbol{u}) = 0$, surface is being sought which is associated with the highest level of joint probability density function. That point geometrically corresponds to the point of tangency between the *limit-state* surface and the constant-$f_u(\boldsymbol{u})$ sphere with the smallest radius, Fig. 1(a). The radius (β) of the sphere is next compared with the corresponding (β_t) and if $\beta < \beta_t$, Fig. 1(a), it implies that the probabilistic constraint is not satisfied (i.e., the multiple integral of the joint probability density function over the fail portion of the *u-space*, $\Phi(-\beta_t)$, exceeds the acceptable level of failure probability, $\Phi(-\beta_t)$).

In the PMA case, the MPP point is found using a different (inverse) formulation. That is, a sphere with radius β_t is constructed and the (MPP) point of tangency with the *limit-state* surface associated with the largest value of the constraining function is sought, Fig. 1(b). If the value of the constraining

relation associated with the MPP is positive, Fig. 1(b) (i.e., if the MPP is located within the *fail* region), the probabilistic constraint in question is violated. In other words, for the MPP point $\beta = \beta_t$ while at the point on the *limit-state* surface which is associated with the largest value of the joint probability density function $\beta \leq \beta_t$, and hence again, the failure probability is greater than the acceptable failure probability, $\Phi(-\beta_t)$.

In the following section, a more detailed description of the PMA method is provided. The RIA is not considered here since it is found to be often associated with high computational cost and/or with a lack of robustness (sometimes simply fails to converge).

2.1.3 Performance Measure Approach. As mentioned above, within the PMA, each of the probabilistic constraints $G(\boldsymbol{u})$ is obtained by first solving the following nonlinear optimization problem in *u-space* (Ref 4-7)

$$\begin{aligned} &\textit{Maximize}: G(\boldsymbol{u}) \\ &\textit{Subjected to}: |\boldsymbol{u}| = \beta_t \end{aligned} \qquad \text{(Eq 2)}$$

to obtain the MPP and then by evaluating the constraining relation at the MPP. Within the optimization procedure, only the direction vector $\boldsymbol{u}_{\beta=\beta_t}/|\boldsymbol{u}_{\beta=\beta_t}|$ needs to be determined due to the use of the *spherical-equality* constraint $|\boldsymbol{u}| = \beta_t$, Eq. 2. Also, rather than employing one of the general-purpose optimization algorithms, PMA optimizations are commonly carried out using the so-called advanced mean value (AMV), the so-called conjugate mean value (CMV), and/or the so-called hybrid mean value (HMV) methods (Ref 11), since these methods do not require a line search. A brief overview of these methods (used in this work) is presented below.

Advanced Mean Value Method. Within the AMV method, the steepest-ascent direction vector, $\boldsymbol{n}(\boldsymbol{u})$ (defined below) evaluated at the MPP, $\boldsymbol{u}_{\text{AMV}}^{(k)}$, is iteratively updated until convergence. The AMV method is, hence, formulated simply as (Ref 11):

$$\begin{aligned} &\boldsymbol{u}_{\text{AMV}}^{(0)} = 0 \text{ and } \boldsymbol{u}_{\text{AMV}}^{(k+1)} = \beta_t \boldsymbol{n}\left(\boldsymbol{u}_{\text{AMV}}^{(k)}\right), \\ &\text{where} \quad \boldsymbol{n}\left(\boldsymbol{u}_{\text{AMV}}^{(k)}\right) = -\frac{\nabla_u G\left(\boldsymbol{u}_{\text{AMV}}^{(k)}\right)}{\left\|\nabla_u G\left(\boldsymbol{u}_{\text{AMV}}^{(k)}\right)\right\|}. \end{aligned} \qquad \text{(Eq 3)}$$

Superscript within parenthesis is used to denote the iteration number, and symbol ∇_u denotes the gradient operator in the *u-space*.

Conjugate Mean Value Method. As shown in Ref 5, then applied to a concave function, the AMV method either tends to converge slowly or become divergent. To overcome these shortcomings of the AMV method, both the current and previous search directions are utilized within the CMV method (Ref 5). Specifically, the new search direction is obtained as a linear combination of three equally weighted steepest-ascent directions: $\boldsymbol{n}(\boldsymbol{u}_{\text{CMV}}^{(k-2)})$, $\boldsymbol{n}(\boldsymbol{u}_{\text{CMV}}^{(k-1)})$, and $\boldsymbol{n}(\boldsymbol{u}_{\text{CMV}}^{(k)})$ (Ref 5). The CMV method is, hence, formulated simply as (Ref 5):

$$\begin{aligned} &\boldsymbol{u}_{\text{CMV}}^{(0)} = 0, \quad \boldsymbol{u}_{\text{CMV}}^{(1)} = \boldsymbol{u}_{\text{AMV}}^{(1)}, \quad \boldsymbol{u}_{\text{CMV}}^{(2)} = \boldsymbol{u}_{\text{AMV}}^{(2)}, \\ &\boldsymbol{u}_{\text{CMV}}^{(k+1)} = \beta_t \frac{\boldsymbol{n}\boldsymbol{u}_{\text{CMV}}^{(k)} + \boldsymbol{n}\boldsymbol{u}_{\text{CMV}}^{(k-1)} + \boldsymbol{n}\boldsymbol{u}_{\text{CMV}}^{(k-2)}}{\left\|\boldsymbol{n}\boldsymbol{u}_{\text{CMV}}^{(k)} + \boldsymbol{n}\boldsymbol{u}_{\text{CMV}}^{(k-1)} + \boldsymbol{n}\boldsymbol{u}_{\text{CMV}}^{(k-2)}\right\|} \quad \text{for} \quad k \geq 2 \end{aligned} \qquad \text{(Eq 4)}$$

where

$$\boldsymbol{n}\left(\boldsymbol{u}_{\text{CMV}}^{(k)}\right) = -\frac{\nabla_u G\left(\boldsymbol{u}_{\text{CMV}}^{(k)}\right)}{\left\|\nabla_u G\left(\boldsymbol{u}_{\text{CMV}}^{(k)}\right)\right\|} \qquad \text{(Eq 5)}$$

The CMV method has been shown to significantly outperform the AMV method relative to the rate of convergence and stability for concave (objective) functions. However, the CMV method was found to be inefficient or unreliable when applied to convex functions.

Hybrid Mean Value Method. To overcome the aforementioned shortcomings associated with the AMV and CMV methods, the HMV method is employed in this work which adaptively selects and utilizes the AMV and CMV methods (depending on the type of the objective function). The first step in that direction is to determine the type (convex versus concave) of the objective function. This is done by employing the steepest-ascent directions at three consecutive iterations as (Ref 5):

$$\textit{Compute}: \varsigma^{(k+1)} = (\boldsymbol{n}^{(k+1)} - \boldsymbol{n}^{(k)})(\boldsymbol{n}^{(k)} - \boldsymbol{n}^{(k-1)}) \qquad \text{(Eq 6)}$$

if $sign(\varsigma^{(k+1)}) > 0$ then the function is convex at $\boldsymbol{u}_{\text{HMV}}^{(k+1)} = 0$ corresponding to $d(X)$ and
if $sign(\varsigma^{(k+1)}) \leq 0$ then the function is concave at $\boldsymbol{u}_{\text{HMV}}^{(k+1)} = 0$ corresponding to $d(X)$.

Once the objective function type is determined, the appropriate optimization method (AMV or CMV) is adaptively selected for the MPP search.

Design Closeness Fast Reliability Analysis. To further accelerate the process of computation of the probabilistic constraints, the so-called design closeness fast reliability analysis is applied (Ref 6). Within this analysis, a design closeness test is conducted at the end of each design iteration. When the two consecutive designs are found to be *close* (which also implies that their respective MPPs are close), then, within the *u-space*, searches for the MPPs in the subsequent design iterations are initiated at the previous iteration MPPs and not at the design variable mean values (i.e., at the *u-space* origin).

Implementation of the RBDO Method. The flow chart used for the implementation of the RBDO method is depicted in Fig. 2. The inner optimization loop associated with determination of the MPP and with the evaluation of the probabilistic constraints and their sensitivities is shown on the left-hand side of Fig. 2. As explained above, evaluation of the probabilistic constraints is similar to that for deterministic constraints except that it is done at the MPP, not at the mean value of the design variables. Since determination of the MPPs entails the solution of the inner-optimization problem, evaluation of probabilistic constraints via the FORMs is computationally quite more expensive than the evaluation of the deterministic constraints. The primary (RBDO) optimization loop is displayed on the right-hand side of Fig. 2. Except for the aforementioned complexities associated with the evaluation of the probabilistic constraints, the RBDO is quite similar to the conventional deterministic design optimization method.

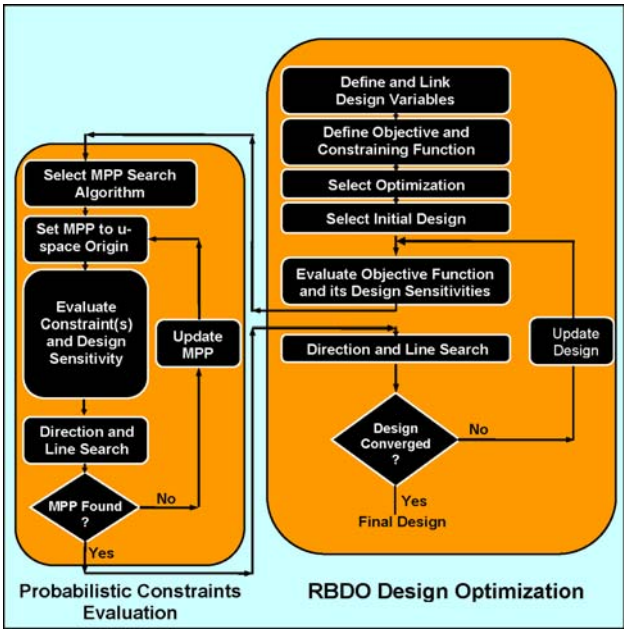

Fig. 2 Flow chart for the reliability-based design optimization (RBDO) employed in this work

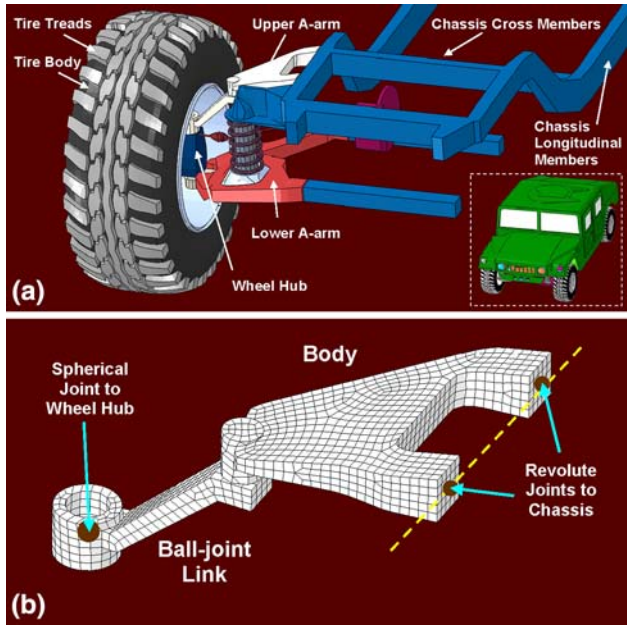

Fig. 3 (a) HMMWV front right A-arm and the adjoining components and (b) a shell-based finite-element model of the front right A-arm used in the fatigue durability analysis

As will be discussed later in greater detail, the objective function in the RBDO problem investigated in this work is the components mass (which must be minimized). The (probabilistic) constraints are related to the fatigue durability life of the component (i.e., with the number of years the component must operate under expected in-service loads before the first detectable cracks are initiated/formed). To avoid dealing with very small or very large values, it is generally convenient to have the performance functions (the probabilistic constraining functions, in this work) be expressed in such a way that their characteristic value is around 1.0. Hence, the probabilistic constraints are expressed as

$$G_i(\boldsymbol{d}(\boldsymbol{X})) = 1.0 - \mathrm{FSL}_i(\boldsymbol{d}(\boldsymbol{X}))/\mathrm{FSL}_t$$

where FSL denotes fatigue strain life, subscript i is the constraint number (the total number of probabilistic constraints is equal to the number of critical locations in the component where fatigue-induced failure has high probability of occurring), and t stands for the targeted value (FSL_t is (arbitrarily) set to 5 years, in this work). The tools used in the evaluation of the objective function, the probabilistic constraints, and data communication between these tools are discussed in next section.

2.2 Fatigue Strain Cycle Controlled Durability

2.2.1 General Determination of In-Service Cyclic Loading. The component analyzed in this work is the front-right upper A-arm (a suspension system component) in the high-mobility multipurpose wheeled vehicle (HMMWV) Model 1025 (up-armored for improved blast/ballistic-threat survivability, Ref 12). This component is displayed both in Fig. 3(a) (along with the adjoining vehicle components) and Fig. 3(b) (in isolation). The component is connected (via two longitudinal revolute joints) to the chassis, on one side, and (via a spherical/ball joint) to the wheel-hub, on the other side, Fig. 3(b).

To determine the (typical) in-service cyclic loads and inertia forces acting on the A-arm, multibody dynamics simulations of the up-armored HMMWV Model 1025 traveling over the Churchville B test track (Ref 13) were carried out. In these simulations, the HMMWV dynamics model consisting of 40 rigid bodies, 40 kinematic joints, and 10 force elements, developed in our prior work (Ref 12), was utilized. Geometrical and kinematic details pertaining to the HMMWV (depicted as inset in Fig. 3a), in general, or regarding the suspension system, specifically, can be found in our recent work (Ref 12).

Multibody dynamics simulations of the HMMWV traveling over the Churchville B test track were carried out at a constant vehicle speed of 30 kph and typically involved 120 s travel duration and a constant integration time step of 0.05 s. These calculations were carried out using SIMPACK, a general purpose multibody dynamics (MBD) package (Ref 14). Details regarding the MBD simulations can be found in our recent work (Ref 12, 15). Topology of the test track was re-created using the power spectral density (PSD) data reported in Ref 13, obtained in tests involving vehicle speed of 2.5 kph.

A total of eight independent in-service (external) loads are considered; three of these (reaction-force type) loads are associated with the spherical joint, whereas the remaining five (three reaction forces and two reaction moments) were associated with one of the revolute joints. It must be noted that, since the A-arm was modeled as a rigid body within the present MBD simulations, only one of two revolute joints connecting this component to the chassis could be modeled to avoid over-constraining the system. (In our ongoing work, the A-arm is being modeled as a flexible body which will allow consideration of both revolute joints. The results of this analysis will be reported in a future communication.)

An example of the time-dependent reaction forces diffusing into the A-arm at its connection points to the adjoining components obtained in this work is displayed in Fig. 4(a) and (b). A quick examination of the cyclic loads displayed in these

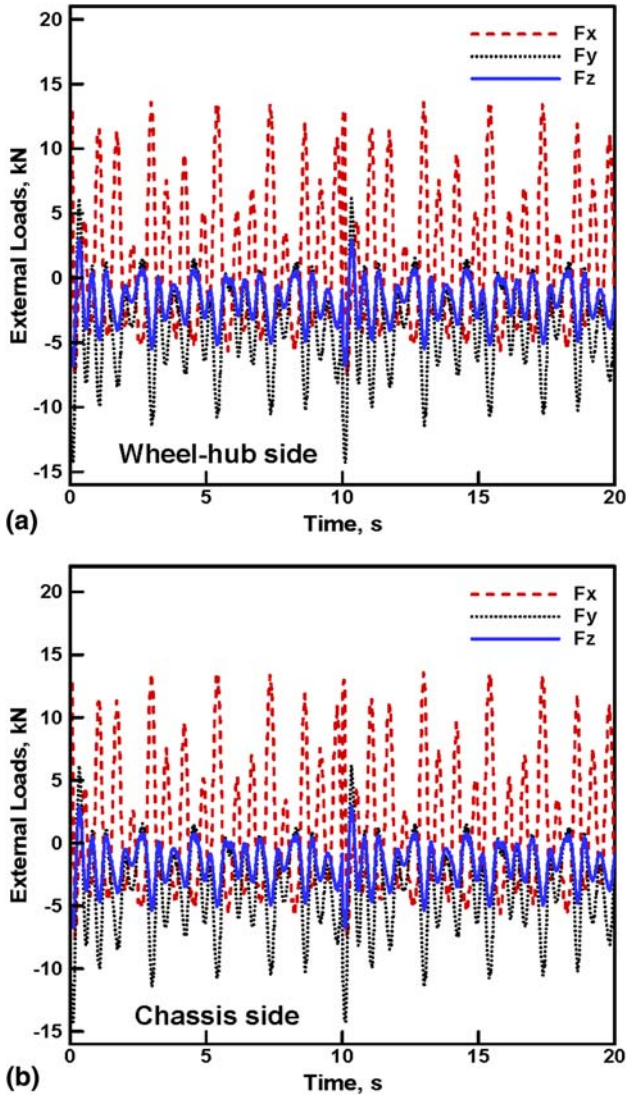

Fig. 4 Typical time-dependent loads diffusing into the A-arm at its connection points to the adjoining components: (a) wheel-hub side and (b) chassis side

figures shows that they are: (a) of a nonconstant amplitude and (b) not in-phase (i.e., loading is *nonproportional*). In addition to considering eight joint reaction forces/moments, three inertia forces and three inertia moments were also considered (the MBD inertia results not shown for brevity).

The aforementioned findings regarding the cyclic loads being of nonconstant amplitude and being nonproportional have important consequences: (a) First, the nonconstant nature of the load amplitude entails the use of a cyclic-counting procedure (e.g., the so-called *Rainflow Analysis*, Ref 16) to represent the (highly irregular) time-dependent loading as a collection of constant amplitude (fixed mean value) loading cycles and (b) Second, since different components of the cyclic loading are not in-phase, not only the magnitudes of the stress/strain components at an arbitrarily selected point in the A-arm are time dependent but also the orientation of the associated principal coordinate system is varying with time. The latter finding is what makes cyclic loading *nonproportional*.

The latter finding further suggests that cycle counting procedure to be employed in this work should classify loading cycles not only with respect to their stress/strain amplitudes and mean values but also with respect to the orientation of their principal coordinate system. Such a procedure is being developed in our on-going work by generalizing the *Rainflow* counting algorithm to include the orientation of the principal coordinate system. Since the finite-element model for the A-arm was based on the use of shell elements (completely wrapping the outer surface of the component and having the appropriate component mass controlled thickness), one of the principal coordinates is taken to be along the local through-the-thickness direction. Hence, the orientation of the local principal coordinate system is defined using a simple in-plane rotation angle with respect to the projected global x-axis (taken to be aligned with the forward vehicle direction). The generalized *Rainflow* algorithm developed will be reported in a future communication. As will be explained in the next section, due to selection of the particular fatigue damage-controlling strain measure (i.e., the von Mises equivalent total strain), capabilities offered by the conventional *Rainflow* analyses were sufficient and enabled completion of this work. Validity of this approach was examined in Section 3 where a more elaborate *critical plane* scheme (Ref 13) was introduced.

2.2.2 Geometrical and Finite-Element Models. As mentioned earlier, a solid model for A-arm is constructed using CATIA V5 CAD program (Ref 17). The model is next meshed using 30 three-node and 1740 four-node first-order shell elements. The elements size was chosen in such a way that stress concentration effects associated with geometrical discontinuities and joints are accounted for explicitly, during the finite-element analyses (FEA) and no stress concentration factors were used. Solid-model preprocessing for the FEA was done using HyperMesh (Ref 18). HyperMesh was also used to define the shape functions, i.e., limiting-shape boundaries within which the critical sections of the component geometry are iterated during the RBDO procedure.

2.2.3 Strain-Life Fatigue Durability Analysis. Due to relatively complicated shape of the A-arm and the presence of associated geometrical stress concentrators and joints, fatigue durability of the A-arm component (displayed in Fig. 3a, b) is expected to be strain controlled. Hence, a strain-life fatigue durability analysis was utilized in this work. In general, a (plastic) strain-life fatigue durability analysis entails specification of the following six relations: (a) the definition of a (scalar) strain measure which governs fatigue-induced damage under multiaxial loading conditions; (b) a strain amplitude, $\Delta\varepsilon/2$, versus the number of cycles to crack initiation, N_f; (c) cyclic stress amplitude, $\Delta\sigma/2$, versus strain amplitude relation; (d) a procedure for including the effect of mean stress/strain; (e) a relationship that can be used to relate elastic stresses and strains (which can be computed very efficiently using elastic finite-element analysis) to their corresponding elastic-plastic equivalents (discussed in more detail below); and (f) definition of a strain-based endurance limit.

Strain Measure Governing Fatigue-Induced Damage. Following Choi and Youn (Ref 6), strain-based fatigue durability is assumed to be controlled by the amplitude of the equivalent total strain, $\Delta\varepsilon/2$. It should be noted that since this quantity is related to the second invariant of the total strain tensor, aforementioned complexities associated with the variation of the orientation of the principal coordinate system during cyclic loading are greatly alleviated.

Strain Amplitude Versus the Number of Cycles to Crack Initiation. The Manson-Coffin-Morrow strain-life relation (Ref 19) was used in this work.

$$\Delta\varepsilon/2 = (\sigma'_f/E)(2N_f)^b + \varepsilon'_f(eN_f)^c \quad \text{(Eq 7)}$$

where E is the Young's modulus, σ'_f is a fatigue-strength coefficient, b is a fatigue-strength exponent, ε'_f is a fatigue ductility coefficient, and c is a fatigue ductility exponent. The latter four quantities represent material-dependant strain-life parameters.

Cyclic Stress Amplitude Versus Strain Amplitude Relation. Assuming a parabolic strain-hardening relation for the material in question, $\sigma = K'(\varepsilon_{pl})^{n'}$, where "pl" denotes plastic, the cyclic strain amplitude versus cyclic stress amplitude relation is defined as:

$$\Delta\varepsilon/2 = (\Delta\sigma/2E) + (\Delta\sigma/2K')^{1/n'} \quad \text{(Eq 8)}$$

where K', a cyclic strength coefficient, and n', is a cyclic strength exponent, are two cyclic-loading material-dependent parameters. It should be noted that the two terms on the right-hand side of Eq 8 represent elastic-strain and plastic-strain amplitudes, respectively. To better understand the relationship between (monotonic) strain hardening and cyclic hysteresis defined by Eq 8, the two relations are shown schematically in Fig. 5(a) and (b). It is clear from Fig. 5(b) that during the first $\Delta\sigma/2$ portion of a loading (half) cycle, material is assumed to relax elastically, whereas during the second $\Delta\sigma/2$ portion, material continues to degrade due to incremental plastic strain.

The Effect of Mean Stress. It is well established that fatigue life is affected not only by the strain amplitude but also by the attendant value of the mean stress (Ref 20). The effect of mean stress is included in this work using the so-called *Morrow correction* (Ref 20) within which σ'_f in Eq 7 is replaced with a $\sigma'_f - \sigma_m$ term, where σ_m is the mean stress. To be consistent with the previously made choice of the strain measure, the equivalent stress was used in the definition of σ_m.

Computation of Elastic-Plastic Stresses/Strains. When analyzing fatigue strain life of the A-arm subjected to complicated cyclic loading, one encounters the challenges of a high computational cost associated with at least the following two reasons: (a) complexities arising for the need for cycle counting which takes into account time dependency of the principal coordinate system and (b) due to the need for carrying out (numerous and computationally costly) elastic/plastic FEA. The first source of high computational cost was eliminated earlier via the use of an orientation-invariant strain measure. To reduce the computing burden associated with the elastic/plastic FEA, the so-called *Neuber's rule* is used (Ref 21) in this work. Within this procedure, the sum of the strain energy and the complimentary strain energy associated with purely elastic and the corresponding elastic-plastic analyses are assumed to be equal. In this way, only computationally efficient purely elastic FEA of the A-arm subjected to the prescribed cyclic loading are analyzed and, via the Neuber's rule, the resulting stresses and strains are converted to their counterparts which would have been obtained if the elastic-plastic FEA were executed.

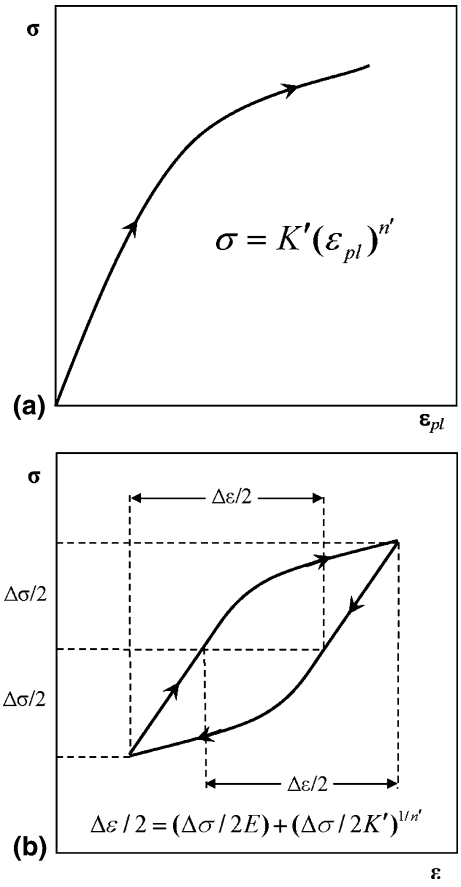

Fig. 5 (a) Monotonic stress-strain parabolic relation and (b) cyclic-hardening stress amplitude vs. strain amplitude relation

Definition of a Strain-Based Endurance Limit. Equation 7 does not provide for a strain amplitude-based endurance limit, i.e., for a maximum strain amplitude below which an infinite strain life is attained. To overcome this deficiency of the strain amplitude versus fatigue life model used, an operational endurance limit is introduced. In accordance with the work of Conle (Ref 22), the endurance limit was set to a 25% of the value calculated from the corresponding stress-life constant amplitude endurance limit as defined in the corresponding *S-N* (i.e., stress amplitude versus number of cycles to failure) curve.

2.3 Computation of the Strain-Life-Based Probabilistic Constraints

The objective of the RBDO introduced in this work is to minimize mass of the upper A-arm while ensuring that the probability for violation of any of the fatigue durability-based constraints $(G_i(\boldsymbol{d}(\boldsymbol{X})) = 1.0 - \mathrm{FSL}_i(\boldsymbol{d}(\boldsymbol{X}))/\mathrm{FSL}_t)$ is lower than a maximum acceptable level of failure probability, $\Phi(-\beta_{t,i})$. In formulating the RBDO problem, the following assumptions were made and the following geometrical-modeling/preprocessing/analysis tools were used:

(a) As mentioned earlier, cyclic and inertia loads were determined via vehicle dynamics simulations using SIMPACK (Ref 14), geometrical modeling of the A-arm was done using CATIA V5 (Ref 17) while preprocessing, including the definition of the shape design variable(s), was done using HyperMesh (Ref 18);

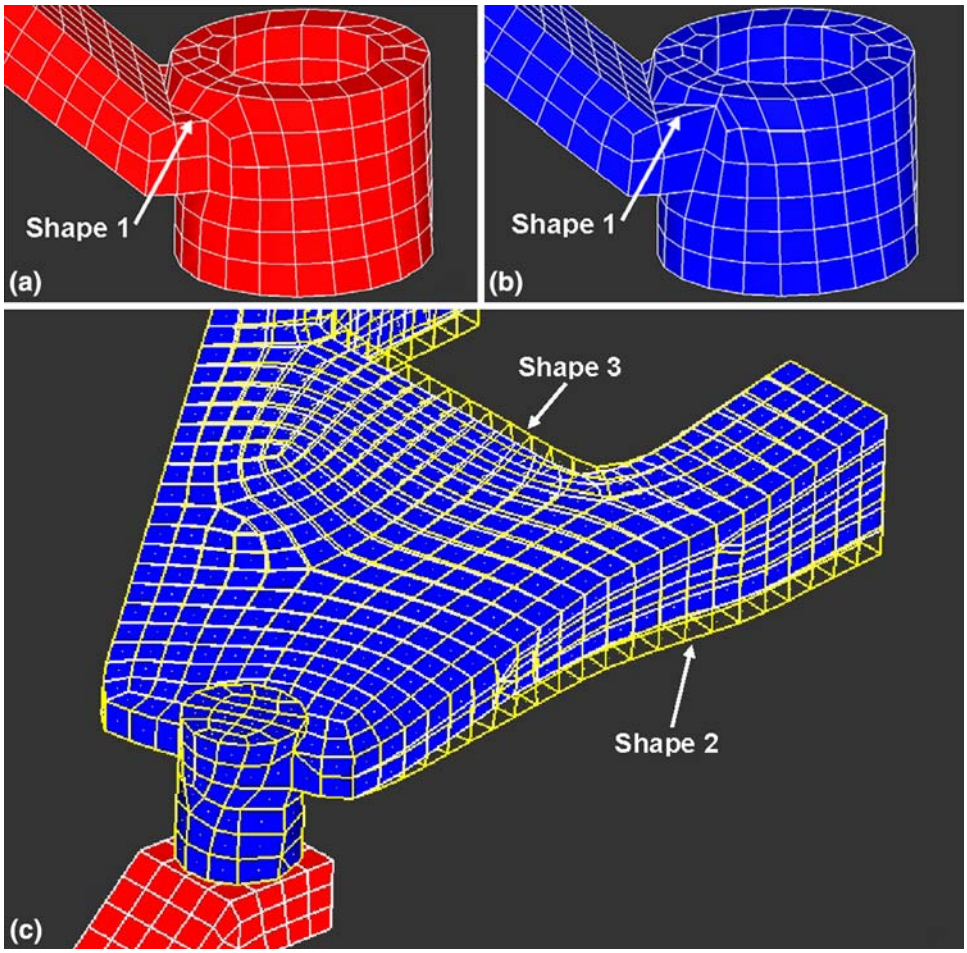

Fig. 6 Three shape functions used in the RBDO of the front right A-arm for the fatigue strain-based durability

(b) To reduce the computational burden, it was assumed that strain life of the component is controlled by the strain life of its most critical elements. These elements were identified in a preliminary fatigue life investigation and it was assumed that the same elements will continue to control strain-induced fatigue failure in the component, as shape and size of the component are being varied during the (global) optimization process in the presence of stochastic variations in the material properties and component geometry/size. Validity of this assumption was confirmed in the final design where it was shown that fatigue durability was also controlled by the same elements/locations in the A-arm. To identify the most critical elements, the procedure for evaluating the strain life (described in greater detail under point (e), below) was applied to all elements in the component;

(c) For simplicity, only three shape and two size design variables are considered while all six fatigue strain-life/cyclic-hardening material parameters are taken to be associated with stochastic variability. The three shape design variables are defined using the Morphing module of HyperMesh and are displayed in Fig. 6(a) to (c). It should be noted that to facilitate understanding of the first shape variable (which effectively introduces chamfer), the initial and the limiting configurations of the affected region are displayed in Fig. 6(a) and (b). Shape variables 2 and 3 are both displayed in Fig. 6(c). Since the upper A-arm under investigation contains two subcomponents (the body and the ball-joint link), shell thicknesses of these two subcomponents are defined as two size variables. The six random fatigue strain-life/cyclic-hardening material parameters considered are listed in Table 1. Stochastic variations of Young's modulus, E, were not taken into account due to the fact that material stiffness is generally considered as being microstructure/processing weakly dependent property. Following the work of Choi and Youn (Ref 6), the shape and the size variables as well as material parameters with negative values (i.e., b and c exponents in Eq. 7) are assumed to be stochastically distributed in accordance with the normal distribution function, whereas (positive) material properties are assumed to be associated with the log-normal distribution. The respective mean values, upper and lower bounds (where applicable), and the coefficient of variance are given in Table 1. Once more, it should be pointed out that only the shape and the size variables are treated as design variables and are iterated during (global) component design-optimization process. On the other hand, both shape/design variables and material parameters are treated as random variables and were considered within the *u-space* and were used in the determination of the MPPs;

Table 1 Definition of random parameters for fatigue strain-life prediction of the upper A-arm made of a AISI-SAE-4340 Steel, SI unit

Parameter	Lower bound	Mean value	Upper bound	Coefficient of variance	Distribution type
Size parameter					
Ball-joint link shell thickness	8.0	8.4	8.8	0.01	Normal
A-arm body shell thickness	6.9	7.9	8.9	0.01	Normal
Shape parameter					
Shape function 1	0.0	0.5	1.0	0.01	Normal
Shape function 2	0.0	0.5	1.0	0.01	Normal
Shape function 3	0.0	0.5	1.0	0.01	Normal
Material parameters					
Cyclic strength coefficient, K'	N/A	1.358×10^9	N/A	0.03	Log-normal
Cyclic strength exponent, n'	N/A	0.12	N/A	0.03	Log-normal
Fatigue strength coefficient, σ'_f	N/A	1.220×10^9	N/A	0.03	Log-normal
Fatigue strength exponent, b	N/A	−0.073	N/A	0.03	Normal
Fatigue ductility coefficient, ε'_f	N/A	0.41	N/A	0.03	Log-normal
Fatigue ductility exponent, c	N/A	−0.60	N/A	0.03	Normal

(d) Computation of the objective function (component mass) was done using ABAQUS/Standard, a general purpose finite-element program (Ref 23);

(e) To compute the strain life of the component, a fairly elaborate scheme was used: (i) First, a series of 14 quasi-static linear-elastic FEA is carried out each associated with a unit load corresponding to one of the eight external loads or six inertia forces/moments, discussed earlier. These analyses yielded 14 sets of stress states for each FEA of the A-arm; (ii) Due to attendant linearity of the problem (at this point), temporal variations of the stress state within each element are obtained by multiplying each of the component stress states obtained in (i) with the corresponding cyclic loading; (iii) Next, the temporal evolution of the equivalent stress and strain are computed for each element using standard linear-elasticity relations; (iv) The Neuber's rule is then invoked and the monotonic-hardening relation, $\sigma = K'(\varepsilon_{pl})^{n'}$, is used to compute the *elastic-plastic* counterparts of the equivalent elastic stress and strains obtained in (iii); (v) Next, the Rainflow cycle counting algorithm is utilized to determine the number of loading (half) cycles of different types, each type being characterized by a unique pair of values of the equivalent stress amplitude and the equivalent stress mean value. The cyclic-hardening relation, Eq 8, is then utilized to convert the equivalent stress amplitudes into equivalent total strain amplitudes. It should be noted that since the Rainflow analysis requires only peak/valley information from the input loading signal, a peak/valley editing procedure had to be applied first to eliminate nonreversal points from the loading signal before the Rainflow analysis could be applied; (vi) For each cycle type, the maximum number of cycles N_f is computed using Eq 7 with the σ'_f term being replaced with $(\sigma'_f - \sigma_m)$ to account for the effect of mean (equivalent) stress, σ_m; (vii) For each cycle type, a ratio of the number of actual cycles in the loading signal is divided by the corresponding number of cycles until failure to determine the associated fractional fatigue strain-induced damage; (viii) Following Miner's rule, the accumulated damage over the time interval equal to the duration of the loading signal is obtained for each element by summing the associated fractional damages obtained in (vi). The finite elements associated with the largest values of the accumulated damage are then identified as the critical elements (i.e., the most likely locations of fatigue-induced failure). The location of the most critical element is indicated in Fig. 7, in which the strain life (in years) is displayed for all elements in the initial design. The fatigue strain life (FSL, defined earlier) is computed for each element by assuming (in accordance with Miner's rule) that the failure (more precisely, nucleation of the surface cracks) will occur when the cumulative damage reaches a value of 1.0. Consequently, FSL for each element is computed by dividing the duration of the input loading signal by the corresponding element cumulative damage; (ix) Once the critical elements are identified, it was assumed that changes in the component design and design variable and material-parameter random variations may affect

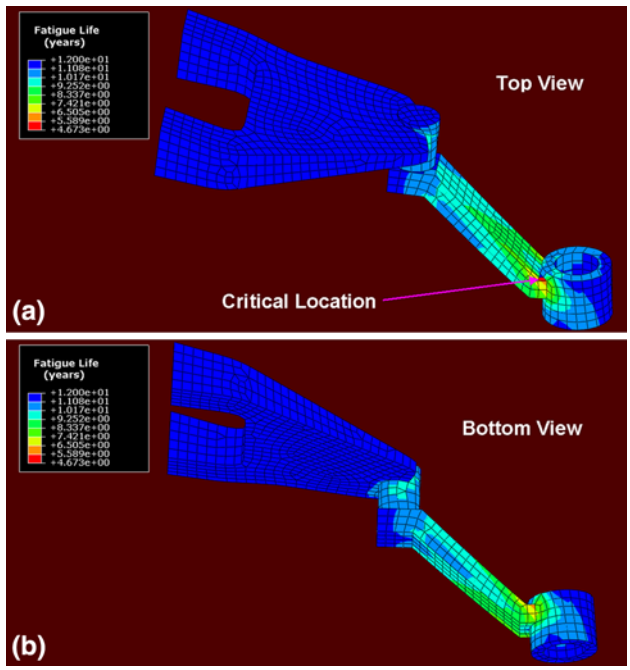

Fig. 7 Fatigue strain-life (in years) distribution over the surface of the front right A-arm: initial design; equivalent strain amplitude-based fatigue life model; confidence level = 0.9987

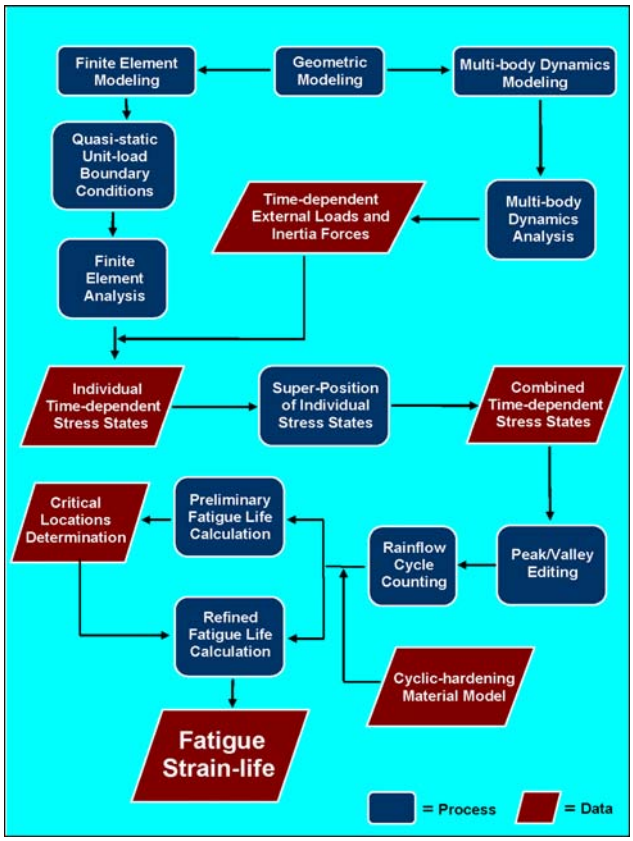

Fig. 8 Flow chart for the computation of fatigue strain life

fatigue strain life but not the location of the fatigue-induced failure. Hence, during the subsequent RBDO process, only the cumulative damage within the critical elements was computed. This greatly reduced the computational cost. To validate the approach used, for the final RBDO-predicted design, cumulative damage is computed for all finite elements in the component. A flowchart depicting the aforementioned procedure for computation of the strain life is provided in Fig. 8.

3. Results and Discussion

The RBDO methodology reviewed in Section 2.1 is combined with the fatigue strain-life assessment procedure discussed in Section 2.2 and integrated with various CAD, MBD, FEA, and general-purpose mathematical (e.g., MATLAB, Ref 24) and engineering optimization programs (HyperStudy, Ref 25) to carry out RBDO of the upper A-arm. Within the RBDO, component weight was used as the objective function (to be minimized) while a desired level of fatigue durability (set to 5 years), at a predefined confidence level of 3-sigma (i.e., $\Phi(3.0) = 0.9987$), for all critical sections of the upper A-arm were used as probabilistic constraints. The main results obtained in this work are presented and discussed in this section.

3.1 Initial Design

To establish a reference case with which all the subsequent results would be compared, the size and shape design variables

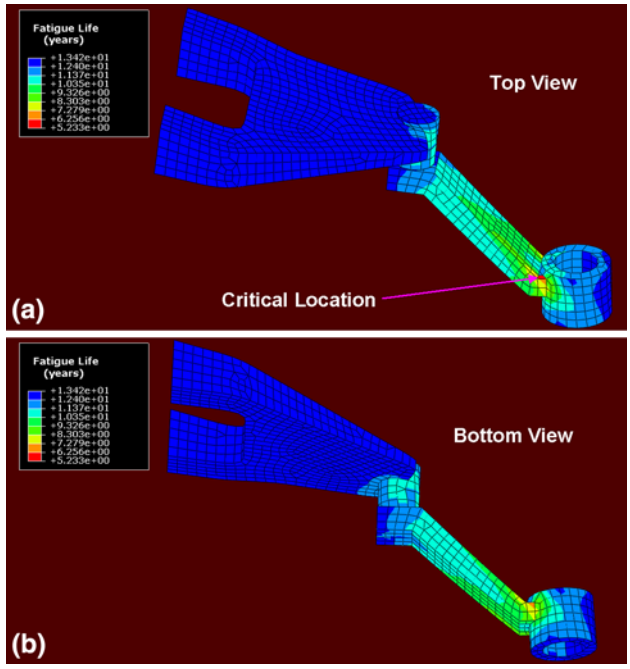

Fig. 9 Fatigue strain-life (in years) distribution over the surface of the front right A-arm: initial design; equivalent strain amplitude-based fatigue life model; deterministic design

and material properties are first set to their (mean) values in the original design and the fatigue strain life computed for all the finite elements in the component. The results of this analysis are displayed in Fig. 9(a) and (b). The location of the most critical element is indicated and the reason that failure is most likely to occur at this location is clearly related to the local geometrical discontinuities (i.e., absence of a fillet radius).

Next, the confidence limit β_t is set to 3-sigma (i.e., failure probability is set to $\Phi(-3.0) = 1.0 - 0.9987 = 0.0013$) and the fatigue strain life is recomputed for all the finite elements in the original design. The results were previously displayed in Fig. 7(a) and (b).

A simple comparison of the results displayed in Fig. 7(a) and (b) with those displayed in Fig. 9(a) and (b) reveals that: (a) the fatigue strain-life values are over predicted in the case when uncertainties in design variables and material properties are not considered and (b) spatial distribution of the fatigue strain life over the component surface in the two cases are quite similar except for a nearly constant scaling factor. Point (a) clearly demonstrates one of the benefits that the RBDO offers over the standard deterministic optimization approaches, since not only the expected (more conservative) fatigue life information is provided but also the confidence level (at which this prediction is made) is defined.

3.2 RBDO-Optimized Design of the Front Right Upper A-Arm

Distribution of the fatigue strain life over the surface of the component at the completion of the RBDO optimization process is displayed in Fig. 10(a) and (b). The RBDO-optimized design displayed is 17% lighter than its counterpart displayed in Fig. 7(a) and (b). It should be noted that further reductions in component weight could have been achieved had the shape function been expanded beyond their current limit

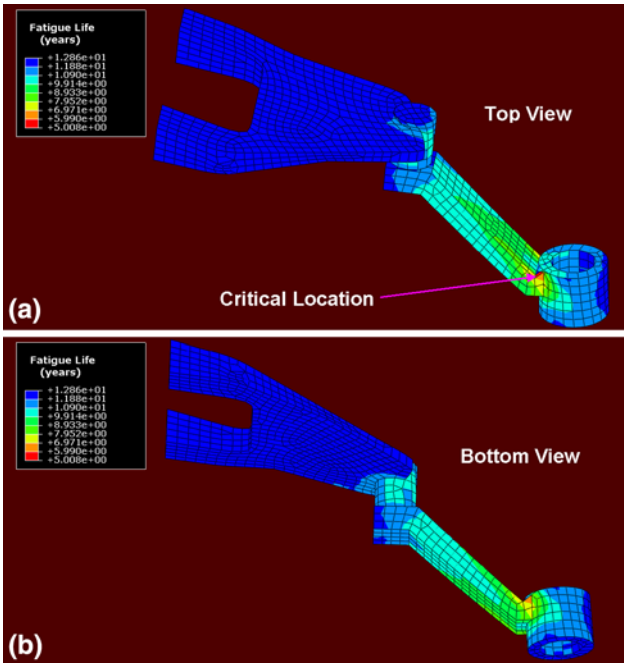

Fig. 10 Fatigue strain-life (in years) distribution over the surface of the front right A-arm: RBDO-optimized design; equivalent strain amplitude-based fatigue life model; confidence level = 0.9987

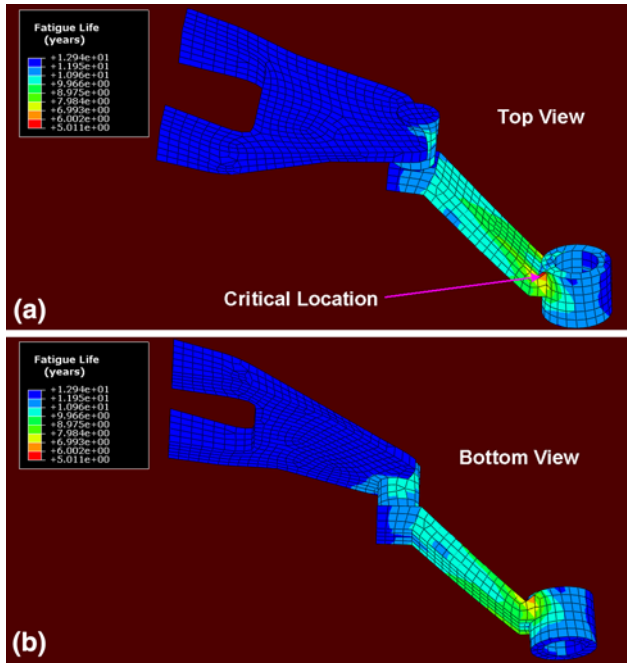

Fig. 11 Fatigue strain-life (in years) distribution over the surface of the front right A-arm: RBDO-optimized design; critical plane-based fatigue life model; confidence level = 0.9987

states. However, this was not done in this work to ensure that the shortest fatigue strain-life sections in the component did not change their location during the RBDO design-iteration process. A comparison of the results displayed in Fig. 10(a) and (b) with their counterparts displayed in Fig. 7(a) and (b) reveals that not only the component weight has been reduced but also the fatigue strain life (at the same confidence level of $\Phi(3.0)$) has improved in the RBDO-optimized design. In fact, in the original design, Fig. 7(a) and (b), some sections are found not to satisfy the (probabilistic) constraints of having fatigue strain life of at least 5 years at a confidence level of 0.9987. Also, the results displayed in Fig. 7(a) and 10(a) show that, as required by the present computational approach, the location of the most critical element has remained unchanged during the optimization process.

3.3 The Effect of Multiaxial Loading

All the calculations of fatigue strain life up to this point were based on the use of Manson-Coffin-Morrow model, Eq 7, with a mean-stress correction. While doing so, the equivalent (total) strain was assumed to be the strain measure controlling crack initiation within the upper A-arm. It is often found that somewhat better prediction of fatigue strain life under multiaxial loading conditions (as is the present case) are obtained if the equivalent strain amplitude in Eq 7 is replaced with the maximum shear-strain amplitude and its conjugate normal-strain amplitude. This procedure requires identification of the so-called *critical plane*, i.e., the plane within each finite element which is associated with the largest sum of the shear-strain amplitude and the conjugate normal-strain amplitude. In addition, to comply with the so-called Brown-Miller multiaxial strain-life fatigue model (Ref 26), the two terms on the right-hand side of Eq 7 are multiplied by 1.65 and 1.75, respectively. Determination of the critical plane is computationally quite costly and, hence, was only applied to the final RBDO design to test validity of the *equivalent strain amplitude* fatigue life model employed in the previous sections. The results of the application of the critical plane-based Brown-Miller multiaxial strain-life fatigue model are displayed in Fig. 11(a) and (b).

A comparison of the results displayed in Fig. 10(a) and (b) with those displayed in Fig. 11(a) and (b) reveals that while the choice of the multiaxial strain-life fatigue model may have some effect (15-20%, in the present case) on the computed values of the fatigue-based durability, the two spatial distributions of strain life over the component surface are quite similar. Hence, it appears justified to use the computationally efficient equivalent strain amplitude-based fatigue durability model during the RBDO process and then to apply the more accurate critical plane model to correct the RBDO-optimized design.

3.4 The Role of Material Property Uncertainties

In the RBDO procedure used up to this point, both manufacturing-induced uncertainties in component size and processing-induced uncertainties in material properties were simultaneously considered. In this section, an attempt was made to separate the effects of these two types/sources of uncertainty. Distribution of the (equivalent strain amplitude-based) fatigue life over the component surface for the RBDO case in which only component size and shape uncertainties are considered is displayed in Fig. 12(a) and (b). A comparison of the results displayed in Fig. 10(a, b) and 12(a, b) shows that material property uncertainties make a significant contribution, causing the fatigue life (at a given level of confidence) to be lowered. This finding suggests that, in the RBDO process, both component size/shape and material property uncertainties should be accounted for.

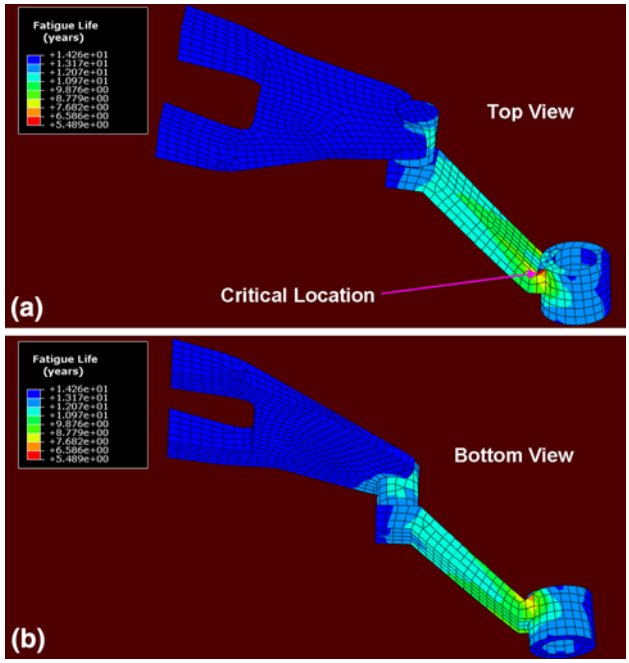

Fig. 12 Fatigue strain-life (in years) distribution over the surface of the front right A-arm: RBDO-optimized design; equivalent strain amplitude-based fatigue life model; confidence level = 0.9987; only shape and size variables uncertainty considered

3.5 Uncertainty Classification

In this work, an attempt was made to include the effects of component manufacturing- and materials processing-induced uncertainties in the component size/shape and its material properties on the optimal design and reliability of a prototypical vehicle suspension system component. One must recognize, however, that, there are other types of uncertainties, in addition to the uncertainties considered in this work. In fact, the following three types of uncertainties are generally recognized (Ref 27-31): (a) uncertainty of the input parameters; (b) model-based uncertainties; and (c) statistical uncertainties. Each of these three types is discussed briefly below.

3.5.1 Input Parameter Uncertainties. This type of uncertainty is generally associated with processing-induced variability in material properties, manufacturing-induced variation in component size and shape, assembly-induced uncertainties in component location/position, uncertainty in the direction and magnitude of in-service loads, etc. In all these cases, the type of distribution (e.g., normal, log-normal, etc.) is assumed to be known and the probability density function in question is then defined in terms of by a set of (predetermined) parameters (e.g., mean, standard deviation, etc.). Also, in the case of material property uncertainties, one must distinguish between *microstructure/processing-insensitive* (more precisely, weakly sensitive) properties (e.g., density, stiffness, etc.) and *microstructure/processing-sensitive* properties (e.g., cyclic-hardening parameters, strain-life parameters, etc.). The former material properties are generally associated with lower levels of uncertainty and are frequently treated as being deterministic. Contrarily, *microstructure/processing-sensitive* properties are generally associated with significant uncertainty and should be treated as stochastic variables.

3.5.2 Model-Based Uncertainties. This type of uncertainty is associated with the mathematical model(s) used to describe various performance aspects of the component in question. For example, in this work, it was assumed that fatigue durability was (plastic) strain controlled, that it can be described by the Manson-Coffin-Morrow relation, Eq 7, and that the equivalent strain amplitude governs the fatigue-induced damage. Since there are other fatigue-based durability models in the literature, there is clearly some uncertainty associated with the strain-life model selected. This type of uncertainty is what is referred to as model-induced uncertainty. In principle, model-induced uncertainties are best quantified through experimental validation/testing. For instance, for the A-arm analyzed in this work it is well established that failure is induced by cyclic loading, that it takes place in the regions near geometrical discontinuities/connection points and that is preceded by plastic deformation.

3.5.3 Statistical Uncertainties. Due to a lack of information/data, frequently there is uncertainty regarding the type of probability density function for the mathematical model parameters. This type of uncertainty is referred to as statistical uncertainties. Manufacturing-induced component shape and size uncertainties are generally found to be associated with normal distributions and a prototypical value of the coefficient of variance (COV, a ratio of the standard deviation and the mean value) of 0.01. Processing-induced material property uncertainties, on the other hand, are generally found to be associated with log-normal distributions with a prototypical COV value of 0.03 (Ref 27-31). When material parameters are negative (e.g., exponents b and c in Eq 7), uncertainty in these parameters is assumed to be governed by the normal distribution functions with COV ≈ 0.03. However, these are only general guidelines and to properly account for this type of uncertainty, experimental tests should be carried out to determine the nature of the associated probability density function as well as the values of the function parameters.

In summary, to fully benefit from the RBDO approach, attention should be paid to all the types/sources of uncertainty and comparable effort should be invested in identifying and quantifying uncertainties before they are utilized. In other words, reliability of the RBDO approach is greatly affected by the quality of input data, in general, and of the parameter, modeling and statistical uncertainties, specifically.

3.6 Potential Benefits of the RBDO

As discussed earlier, substantially reduced weight of future tactical and battle vehicles is one of the major challenges facing the U.S. military. It is critical that any weight reduction does not seriously compromise either the blast/ballistic-threat resistance and survivability of the vehicles or their in-service durability and reliability. The use of the RBDO can provide important guidelines in vehicle-light weighting efforts.

The following simple qualitative analysis can be used to understand the role that the RBDO approach can play in military-vehicle light-weighting efforts. In general, increasing component size (and weight), i.e., applying a safety factor, can be used to lower in-service cyclic stresses experienced by the component. However, this is counterproductive with respect to the attainment of lower vehicle weight. In addition, the safety-factor values are selected quite arbitrarily and, consequently, are often overly conservative. This may lead to either unnecessarily oversized or unreliable prone-to-failure components.

What the RBDO offers is the ability to set component performance/reliability goals (e.g., the component should last no longer than the expected vehicle life and this targeted component life should be guaranteed at a predefined confidence level). In this way, a compromise is struck between the component shape and size/weight, on one hand, and its durability/reliability, on the other. In these efforts, identification and quantification of the type and extent of uncertainty in material properties are highly critical.

4. Summary and Conclusions

Based on the results obtained in this work, the following main summary remarks and conclusions can be drawn:

1. Light weighting (by size reduction and shape changes) of a prototypical suspension system component in a HMMWV subjected to ensuring the expected in-service component life (governed by low cycle strain-based fatigue) is investigated in the presence of component manufacturing- and material processing-induced variability in component size/shape and material properties.
2. The computational approach utilized entailed integration of geometric modeling and preprocessing tools, RBDO methods, finite element analyses, strain-life assessment procedures, and material databases into a complex multi-threaded computational algorithm.
3. The results obtained revealed that the presence of the component size/shape uncertainties as well as of the material property uncertainties can significantly affect component fatigue-based durability.
4. Potential benefits of the *RBDO* approach in helping the U.S. military attain its goal of making their tactical and battle fleets more mobile, deployable, and sustainable are also addressed.

Acknowledgment

The material presented in this article is based on work supported by a research contract with the Automotive Research Center (ARC) at the University of Michigan and TARDEC.

References

1. I. Enevoldsen and J.D. Sorensen, Reliability-Based Optimization in Structural Engineering, *Struct. Saf.*, 1994, **15**, p 169–196
2. X. Yu, K.K. Choi, and K.H. Chang, A Mixed Design Approach for Probabilistic Structural Durability, *J. Struct. Optim.*, 1997, **14**(2–3), p 81–90
3. D.M. Frangopol and F. Moses, Reliability-based structural optimization, *Advances in Design Optimization*, Chap. 13, H. Adeli, Ed., Chapman & Hall, London, 1994, p 492–570
4. J. Tu and K.K. Choi, A New Study on Reliability-Based Design Optimization, *ASME J. Mech. Des.*, 1999, **121**(4), p 557–564
5. B.D. Youn, K.K. Choi, and Y.H. Park, Hybrid Analysis Method for Reliability-Based Design Optimization, *ASME J. Mech. Des.*, 2003, **125**(2), p 221–232
6. K.K. Choi and B.D. Youn, On Probabilistic Approaches for Reliability-Based Design Optimization, *9th AIAA/NASA/USA/ISSMO Symposium on Multidisciplinary Analysis and Optimization*, Sept 4–6, 2002 (Atlanta, GA), 2002
7. K.K. Choi and B.D. Youn, Investigation of the Nonlinearity of Reliability-Based Design Optimization, *28th ASME Design Automation Conference*, Sept 30-Oct 2, 2002 (Montreal, Canada), 2002
8. H.O. Madsen, S. Krenk, and N.C. Lind, *Methods of Structural Safety*, Prentice-Hall, Englewood Cliffs, NJ, 1986
9. T.C. Palle and J.B. Michael, *Structural Reliability Theory and Its Applications*, Springer-Verlag, Berlin, 1982
10. H.O. Fuchs and R.I. Stephens, *Metal Fatigue in Engineering*, John Wiley & Sons, New York, 1980
11. Y.T. Wu, H.R. Millwater, and T.A. Cruse, Advanced Probabilistic Structural Analysis Method for Implicit Performance Functions, *AIAA*, 1990, **28**(9), p 1663–1669
12. M. Grujicic, G. Arakere, H. Nallagatla, W.C. Bell, and I. Haque, Computational Investigation of Blast Survivability and Off-road Performance of an Up-armored High-Mobility Multi-purpose Wheeled Vehicle (HMMWV), *J. Automob. Eng.*, 2008, accepted for publication
13. M.D. Letherwood and D.D. Gunter, Spatial Multibody Modeling and Vehicle Dynamics Analysis of a Future Tactical Truck System Concept, *Proc. SPIE*, 2004, **5423**, p 276–287
14. SIMPACK Version 8900, *User Documentation*, Intec Inc., Indianapolis, IN, 2008
15. M. Grujicic, H. Marvi, G. Arakere, W.C. Bell, and I. Haque, The Effect of Up-armoring the High-Mobility Multi-purpose Wheeled Vehicle (HMMWV) on the Off-road Vehicle Performance, *Multidiscip. Model. Mater. Struct.*, 2009, submitted for publication
16. M. Matsuishi and T. Endo, Fatigue of Metals Subjected to Varying Stress, *Proceedings of Kyushu Branch of JSME* (Fukuoka, Japan), 1968, p 37–40
17. *CATIA V5*, Dassault Systemes Inc., Vélizy-Villacoublay, France, 2009
18. *Altair HyperMesh*, Altair Engineering Inc., Troy, MI, 2009
19. S.S. Manson, Fatigue: A Complex Subject—Some Simple Approximations, *Exp. Mech.*, 1965, **5**, p 193–226
20. J.D. Morrow, Fatigue Properties of Metals, *Fatigue Design Handbook*, Chap. 3.2, Society of Automotive Engineers, Warrendale, PA, 1968
21. H. Neuber, Theory of Stress Concentration of Shear Strained Prismatic Bodies with Arbitrary Non-Linear Stress-Strain Law, *J. Appl. Mech.*, 1961, **28**, p 544–550
22. A. Conle and T.H. Topper, Overstrain Effects During Variable Amplitude Service History Testing, *Int. J. Fatigue*, 1980, **2**(3), p 130–136
23. ABAQUS/Standard Version 6.8-1, *User Documentation*, Dassault Systemes, Providence, RI, 2008
24. MATLAB, *The Language of Technical Computing*, 7th ed., The MathWorks Inc., Natick, MA, 2006
25. *HyperStudy, User Manual*, Altair Engineering Inc., Troy, MI, 2007
26. F.A. Kandil, M.W. Brown, and K.J. Miller, Biaxial Low Cycle Fatigue Fracture of 316 Stainless Steel at Elevated Temperatures, *Mechanical Behaviour and Nuclear Application of Stainless Steels at Elevated Temperatures*, **B280**, The Metals Society, London, 1982
27. K.K. Choi, J. Tang, E. Hardee, and B.D. Youn, "Application of Reliability-Based Design Optimization to Durability of Military Vehicles," SAE International, 2005-01-0530, 2005
28. D.T. Rusk and P.C. Hoffman, Component Geometry and Material Property Uncertainty Modeling for Probabilistic Strain-Life Fatigue Predictions, *6th Joint FAA/DoD/NASA Aging Aircraft Conference*, Sept 16-19, 2002 (San Francisco, CA), 2002
29. K.K. Choi and B.D. Youn, Reliability-Based Design Optimization of Structural Durability Under Manufacturing Tolerances, *Fifth World Congress of Structural and Multidisciplinary Optimization*, May 19-23, 2003 (Lido di Jesolo, Venice, Italy), 2003
30. B.D. Youn and K.K. Choi, A New Response Surface Methodology for Reliability-Based Design Optimization, *Comput. Struct.*, 2004, **82**, p 241–256
31. R. d'Ippolito, M. Hack, S. Donders, L. Hermans, N. Tzannetakis, and D. Vandepitte, Improving the Fatigue Life of a Vehicle Knuckle with a Reliability-Based Design Optimization Approach, *J. Stat. Plan. Inference*, 2009, **139**, p 1619–1632